Behavior of strain stripe networks in barium titanate nanocrystals on crossing its ferroelectric phase transition

Jiecheng Diao [1,2] Longlong Wu [3] Ana F. Suzana,[3] Emil S. Bozin [3] Edoardo M. Zatterin,[4] Steven J. Leake [4]
Ross J. Harder,[5] Wonsuk Cha,[5] Milinda Abeykoon,[6] Jiadong Fan,[2] Huaidong Jiang,[2] and Ian K. Robinson[1,3,*]

[1]*London Center for Nanotechnology, University College London, London WC1E 6BT, United Kingdom*
[2]*Center for Transformative Science, ShanghaiTech University, Shanghai 201210, China*
[3]*Condensed Matter Physics and Materials Science Division, Brookhaven National Laboratory, Upton, New York 11973, USA*
[4]*ESRF–The European Synchrotron, 71 Avenue des Martyrs, Grenoble 38000, France*
[5]*Advanced Photon Source, Argonne National Laboratory, Lemont, Illinois 60439, USA*
[6]*Photon Sciences Division, Brookhaven National Laboratory, Upton, New York 11973, USA*

Nanoscale strain networks are reported in BaTiO$_3$ (BTO) crystals of 300 nm size using Bragg coherent diffractive imaging. BTO nanocrystals with clear facets were chosen to identify the crystallographic directions, allowing the strain field direction and periodicity to be studied in detail. Stripes of strain were observed, which were both stable and preserved in tetragonal and cubic phases at elevated temperatures, above the tetragonal-to-cubic phase transition. A finite element analysis approach was used to simulate the domain structures inside a BTO crystal and to understand the origins of the strain stripes as piezoelectric blocks. A 180° domain model gives a better qualitative match to the experimental images.

I. INTRODUCTION

Barium titanate (BTO) is a ferroelectric material with a large dielectric constant, which is widely used in the electronics industry [1,2]. From low to high temperature, most ferroelectrics would go from low symmetry to high symmetry lattices, although in some cases the highest symmetry phase is not achieved before the melting point. BTO is one of the longest-known ferroelectrics with an ABO_3 perovskite structure, where the Ti^{4+} cations sit at B sites inside an O^{2-} octahedral shell. It has a rhombohedral lattice (trigonal crystal system, R3m) at the lowest temperature, orthorhombic lattice (B2mm) at $-70\,°C$, and tetragonal lattice (P4mm) at $5\,°C$, and finally a cubic lattice (Pm3m) at $120\,°C$ [3,4]. It also shows hysteresis, with a gap in transition temperature between heating and cooling. Such a transition delay, seen also in glasses, is understood to imply a first-order transition, where the system needs time and activation energy to complete the transition. In BTO, the activation is believed to come from disorder associated with the different alignments of spontaneous polarizations [5–7].

The ferroelectricity in BTO arises from the symmetry breaking in the crystal lattice, where there is a delicate balance between long-range Coulomb force and short-range repulsion

[8,9]. In the tetragonal phase, the Ti^{4+} and Ba^{2+} cations are shifted along the c axis relative to the O^{2-} ions, which results in a spontaneous polarization along the c axis in a single unit cell. These polarizations in unit cells could align together to lower the energy of the system and form domains separated by 90° or 180° domain walls. These structures are stabilized by a pair of competing energies, the energy cost of the domain wall formation and the electrostatic energy gain from domain formation [10]. Pure ferroelectric domain walls separate 180° domains, where the polarizations between adjacent domains are antiparallel to each other. The ferroelastic domain walls are also ferroelectric but involve changes of elastic strain upon formation as seen in 90° domains. The ferroelastic domain walls are structurally the same as twin boundaries, where the two adjacent domains have mirror symmetry near the domain wall [11].

The particle size also makes a big difference and variations in size result in distinct properties like different tetragonality, Curie temperature and dielectric constant [12–15]. For BTO nanoparticles, instead of standard 90° or 180° domains, other structures were also proposed for the tetragonal phase. For example, a core-shell model was proposed to explain the residual diffraction signals between (101) and (110) peaks in powder x-ray diffraction experiments [16–18]. Local orthorhombic and rhombohedral structures were found by x-ray and neutron pair distribution function (PDF), although the global structure remains tetragonal [19–22].

Bragg coherent diffraction imaging (BCDI) is a powerful x-ray technique for investigating the structures of individual nanocrystals in three dimensions on the 30-nm resolution scale using the coherence provided by third and fourth generation synchrotrons. The advantage of BCDI is its high

---

[*]Corresponding author: i.robinson@ucl.ac.uk

sensitivity to the distribution of nanoscale strains inside the nanocrystal under investigation [23–27]. In this work, BCDI was used to explore the internal strain distributions in BTO nanocrystals, where unexpected strain stripes were explored and quantified.

II. EXPERIMENTAL METHODS

Commercial BTO particles with mean size of 200 nm were obtained from Santa Cruz Biotechnology [28]. For BCDI measurements, these commercially obtained BTO particles were suspended in ethanol solution with 1% tetraethyl orthosilicate before drop-casting onto silicon wafers and calcining at 700 °C in air for 1 h. After calcination, the BTO samples were put onto the sample stage at Advanced Photon Source (APS) 34-ID-C for an *ex situ* BCDI experiment. The 9-KeV x-ray beam was made coherent by 70 × 30-micron slits and then focused by Kirkpatrick-Baez mirrors to 690 nm(H)×450 nm(V) to illuminate a small number of the crystals. The Medipix detector, with 55 μm pixels, was set to the {110} Bragg angle and placed 0.5 m away from the sample stage to satisfy the oversampling condition for far-field imaging [29]. During the experiment, the incidence angle on the substrate was between 3° and 5° to have an extended x-ray footprint to help find suitable crystal peaks. Once a peak was identified, the chosen crystal was centered in the beam using piezodriven nanopositioners.

The *in situ* BCDI experiment with elevated temperature was performed at the European Synchrotron Radiation Facility (ESRF) ID01 beamline. The sample was heated in the ID01 furnace. It consists of a resistive heater with the heating element being in contact with an alumina crucible, on top of which the sample is pasted. It has two thermocouples, one inside the bulk of the crucible and an external one which is then attached as close as possible to the sample. The output of the first thermocouple is fed into a PID controller (Eurotherm) that regulates the power applied to the heater. The output of the second thermocouple is logged by the beamline computer and recorded as the sample temperature in this work. The furnace's PID parameters were calibrated using this second external thermocouple. To minimize the effort of tracking crystals upon subsequent heating, the samples were heated directly to 100 °C and kept at this temperature. A small number of selected crystals were then tracked while heating in 5 °C steps to 160 °C, well above the tetragonal-cubic phase transition temperature of bulk BTO. The crystals were then cooled down with the same 5 °C steps. At each temperature step during heating and cooling, the temperature would be kept for 30 min before the BCDI measurements were carried out. To make sure the center of the crystals was preserved, position alignment scans were carried out before each BCDI measurement. The incident x-ray energy was set to 10.35 KeV, which corresponds to a wavelength of 1.1979 Å. The focus size at the sample stage was 1.2 μm(H) × 750 nm(V). For the commercial BTO samples at room temperature, the (110) powder ring sits at 24.51° and the (101) powder ring locates at 24.39°. When heated up, the a and c lattice constant of BTO would become closer, and so would the angles of the (110) and (101) powder rings. The two-dimensional (2D) Maxipix detector was placed 0.546 m away from the sample stage with

a pixel size of 55 μm. The scanning step size (dth) of the rocking curve scan was chosen to match the crystal size. For a typical 300-nm BTO crystal, a scanning step size of 0.02° was chosen.

Once the diffraction patterns were recorded, data processing were carried out to exploit the underlying information inside the crystals. Because only the intensity of diffraction pattern was recorded, which is the square of the amplitude. The missing phase information could be retrieved through iterative phasing algorithms [30,31]. In this experiment, the diffraction patterns were reconstructed by carefully choosing the phase retrieval algorithms and adjusting the corresponding parameters of algorithms. The algorithms employed were a combination of error reduction, difference map, relaxed averaged alternating reflections, hybrid projection reflection, and averaged successive reflection [31–35]. Apart from these phase iterative algorithms, the guided algorithm approach is also applied, in which the iterative phasing was run in five parallel populations with five generations. The return matrices and breeding mode are optimized. The reproducibility of the results is confirmed by quantitatively comparing the reconstruction results from random seeding. Further details of the reconstruction refinement are included in Supplemental Material A (SMA) [36].

III. POLAR DOMAINS IN TETRAGONAL BARIUM TITANATE NANOCRYSTALS AT ROOM TEMPERATURE

In the BCDI experiment, every Bragg peak could be used to reconstruct the sample shape and calculate the projected strain onto the Q vector. However, it is necessary to measure three noncoplanar reflections to resolve all the crystallographic directions and hence image the full strain tensors within a selected crystal grain. In this work, the BTO nanocrystals are randomly distributed on the silicon wafer and the x-ray beam can hit more than one crystal at a time. It is more efficient to measure only one Bragg reflection of the ensemble of crystals naturally available in a powder sample. In such cases, without a secondary reference reflection, the crystallographic orientations of the measured crystal are unknown. The only known direction is that of the **Q** vector, which is determined by the direction of the incident and diffracted x-ray beam in experiment and denotes the corresponding crystallographic Bragg reflection.

The measured diffraction pattern was reconstructed to the real space crystal through the phase retrieval algorithms as elaborated in the SMA. After the error matrices were minimized, the reconstructed crystal was converged and showed good reproducibility among different seedings. The **Q** direction is available in the final image in the real space coordinates, which is given by

$$\boldsymbol{Q} = \boldsymbol{k}_f - \boldsymbol{k}_i = k_0[\sin\delta\cos\gamma, \ \sin\gamma, \ \cos\delta\cos\gamma - 1]. \quad (1)$$

The $\boldsymbol{k}_i$ and $\boldsymbol{k}_f$ are the wave vector of the incident and the diffracted x-ray beam, respectively. $k_0 = \frac{2\pi}{\lambda}$ is the corresponding angular wave number and λ is the wavelength of the incident x-ray. The δ and γ are the detector horizontal and vertical angles. Given that the only direction known in the final image is the Q vector, to retrieve the correct crystallographic axes, at least two noncollinear crystal directions are needed. In
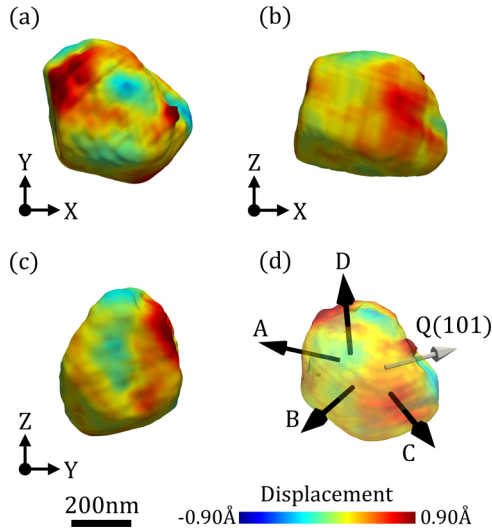
FIG. 1. Different views of the BCDI reconstruction of one representative BTO crystal showing clear crystal facets. (a)–(c) Three orthogonal views of the crystal shape in laboratory coordinates of the experiment. (d) The facets are marked with black arrows, while the Q vector is denoted by a grey arrow.

this work, the additional information comes from identifying and calibrating the angles between the crystal facets of BTO sample.

Figure 1 shows the reconstructed BTO crystal in different views from the BCDI experiment. Figures 1(a)–1(c) show three orthogonal views of one BTO crystal in laboratory coordinates. Several flat facets are observed and labeled A, B, C, and D in Fig. 1(d). The **Q** vector is also plotted, which is known to be the crystallographic (101) or (011) direction. Since for tetragonal structure (101) is equivalent to the (011) direction, the **Q** vector is denoted as (101) for simplicity.

In the BCDI experiment, small variation of the positions of the lattice planes would cause an optical path length difference (phase) of the coherent diffracted x-ray beam, which then goes into the diffraction pattern [23]. By measuring this phase variation, the displacement of the lattice plane can be quantified, which are shown as the color in Fig. 1.

Surface free energy arguments favor the facetting of single crystals along "low-index" directions where the surface atoms are more close-packed [40]. From low temperature to high temperature, BTO has rhombohedral, orthorhombic, tetragonal, and cubic structure, respectively. The two lowest temperature structures should not be present in our experiments, but are believed to exist in the local structure [12–15] and in certain nanoparticle models [16–18]. All these crystal structures tend to have pseudocubic {100}, {110}, and {111} facets. To index the facets, their direction cosines were measured in Paraview and used to calculate all the interfacet angles in Table I [41]. The reference angles between pseudocubic {100}, {110}, and {111} are also presented.

Both facets A and B lie at the {111}/{110} reference angle from the **Q** vector, so must be {111}. Facet C has the {111}/{100} characteristic angle with both A and B so must be {100}. For crystallographic consistency, we label Facet A as (111), then facet B, C, D as (−11−1), (010) and (10−1), respectively. This procedure allows all the crystallographic directions to be established.

To explore the inner information inside the crystal, slices were taken along crystallographic planes. Fig. 2 shows 5 slices across the crystal, perpendicular to the crystallographic (100) direction. Slice 3 is the central slice through the crystal geometric center, while the other slices are separated by 50 nm. The initial phase images from the reconstruction were converted to the strain field by taking derivatives of the phase along each of the three crystallographic axes with normalization. Because the strain field derived from the phase image represents a projection onto the **Q** vector, they correspond to

TABLE I. Interfacet angles between facets and the **Q** vector of crystal in Fig. 1.

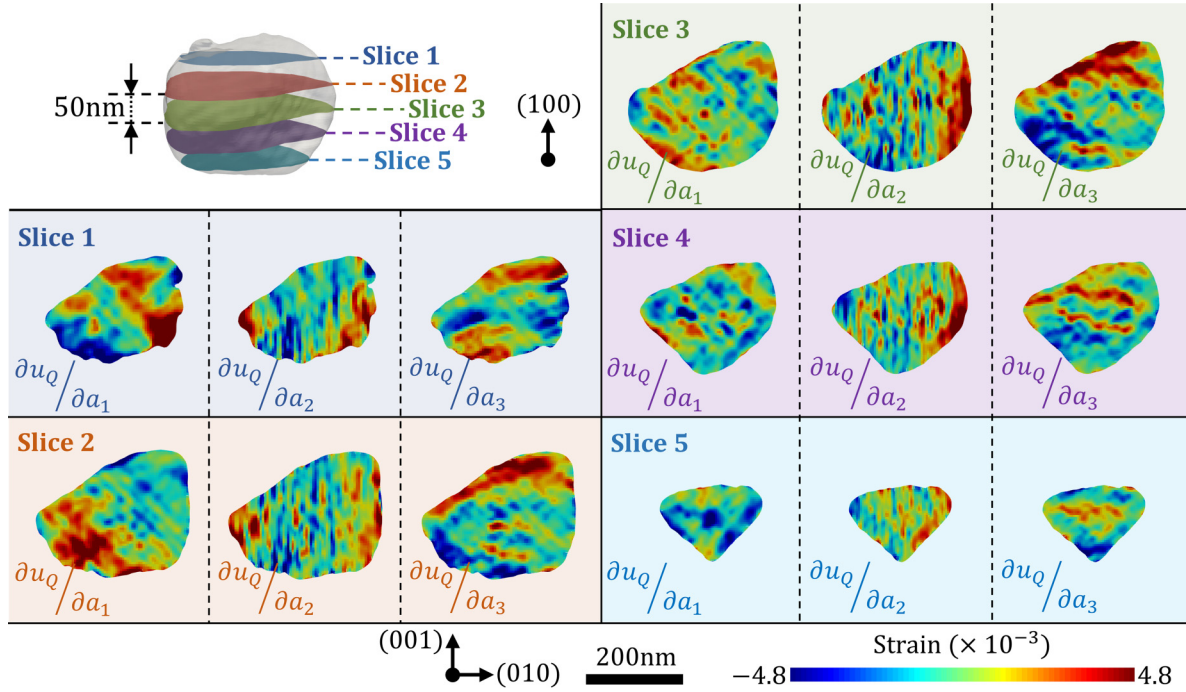|	A	B	C	D	Q	{100}	{110}	{111}
A		109.0°	54.4°	90.6°	35.6°	-	-	-
B	-		54.7°	90.4°	144.6°	-	-	-
C	-	-		89.0°	90.0°	-	-	-
D	-	-	-		90.5°	-	-	-
Q	-	-	-	-		-	-	-
{100}	-	-	-	-	-	90.0°	45.0°/90.0°/135.0°	54.7°/125.3°
{110}	-	-	-	-	-	-	60.0°/90.0°/120.0°	35.3°/90.0°/144.7°
{111}	-	-	-	-	-	-	-	70.5°/109.5°

FIG. 2. Five (100) slices (from Slice 1 to Slice 5) with a 50 nm gap were cut through the crystal to show the strain gradient inside.

the following linear combinations of strain tensors:

$$\frac{\partial u_{101}}{\partial a_1} = \frac{\partial (u_{100}\cos 45° + u_{001}\cos 45°)}{\partial a_1} = \frac{\sqrt{2}}{2}(\varepsilon_{11} + \varepsilon_{31}), \tag{2}$$

$$\frac{\partial u_{101}}{\partial a_2} = \frac{\partial (u_{100}\cos 45° + u_{001}\cos 45°)}{\partial a_2} = \frac{\sqrt{2}}{2}(\varepsilon_{12} + \varepsilon_{32}), \tag{3}$$

$$\frac{\partial u_{101}}{\partial a_3} = \frac{\partial (u_{100}\cos 45° + u_{001}\cos 45°)}{\partial a_3} = \frac{\sqrt{2}}{2}(\varepsilon_{13} + \varepsilon_{33}). \tag{4}$$

Here, the u_{101} and u_{100} are the displacement field along (101) and (100) direction, while the $\varepsilon_{ij}(i, j = 1, 2, 3)$ denotes the strain tensors. Each derivative of the displacement over the crystallographic (100) and (001) directions contains the sum of a normal strain tensor and a shear strain tensor, while the derivative over the (010) direction only contains the sum of two shear strain tensors.

Figure 2 shows the derivatives of the projected displacement fields along all three crystallographic directions in Slices 1 to 5, which are the strain components listed in Eqs. (2) to (4). From the slice images, there are stripes roughly 45° in the derivatives along the crystallographic (100) and (001) directions, but 90° in the derivatives along the (010) direction. These "strain stripes" appear in all the Slices from 1 to 5, which indicates the presence of strain stripes all over most of the central 300 nm of the crystal volume.

Following the same procedure, slices 6 to 10 were prepared perpendicular to (010) direction, and slices 11 to 15 perpendicular to (001) direction. The strain tensor components in these slices are shown in Supplemental Material B.

We then used autocorrelation functions (ACFs) as a mathematical tool to quantify the periodicity and direction of the strain stripes. The correlation coefficients are the measurements of the dependence of the two variables. The widely used Pearson correlation coefficient r, between two data sets x and y, applied to the sample of n measurements, has the definition

$$r = \frac{\sum_{i=1}^{n} (x_i - \bar{x})(y_i - \bar{y})}{\sqrt{\sum_{i=1}^{n} (x_i - \bar{x})^2 \sum_{i=1}^{n} (y_i - \bar{y})^2}}. \tag{5}$$

The x_i and y_i are the *i*th measurements, while the $\bar{x}$ and $\bar{y}$ are the sample means. The Pearson correlation coefficient has a value range from −1 to 1. The value 1 means the two variables are perfect correlated positively, and the −1 means a perfect negative correlation. The value 0 means no correlation between the two.

Different correlations could be defined from the Pearson correlation.

If the two input variables x_i and y_i in Eq. (5) are the same variable with different delay or shifting, then the ACF is set up using the same formula as the Pearson correlation coefficient [42,43]. Here we use the normalized 1D ACF r_{ACF} to describe the strain stripes as a function of shift distance, d, as

$$r_{ACF-1D}(d) = \frac{\sum_{i=1}^{D} (S_0 - \bar{S})(S_{i+d} - \overline{S_{i+d}})}{\sqrt{\sum_{i=1}^{D} (S_i - \bar{S})^2 \sum_{i=1}^{D} (S_{i+d} - \overline{S_{i+d}})^2}}, \tag{6}$$

where S_0 and S_d are the strain gradient at zero position and the shifted position, respectively, and $\bar{S}$ is the mean value of the strain gradient.

Similarly, the 2D autocorrelation function can also be defined for an image or a 2D array. For the array size of $m \times n$, the 2D ACF could be defined as

$$r_{ACF-2D}(d_x, d_y) = \frac{\sum_{i=1}^{m} \sum_{i=1}^{n} (S(i,j) - \bar{S})(S(i+d_x, j+d_y) - \bar{S})}{\sqrt{\sum_{i=1}^{m} (S(i,j) - \bar{S})^2 \sum_{i=1}^{n} (S(i+d_x, j+d_y) - \bar{S})^2}},$$ (7)

where d_x and d_y are the movement in x and y direction, respectively. $S(i,j)$ is the strain gradient at point (i,j) and $\bar{S}$ is the mean value.

Selected regions from the slices in Fig. 2 were used to calculate the 2D ACF using Eq. (7). Figure 3 shows the 100 nm × 100 nm areas that cropped from a typical area in Slice 3 in Fig. 2. Figure 3(a) shows the enlarged view of strain gradient in (100) direction. Correspondingly, Fig. 3(b) shows the 2D ACF result of this strain gradient distribution along the (100) direction, which is pointing out of the plane. There are also weak correlations along the (011) direction, which is obvious when observing the slice view in Fig. 3(a). The strong correlation happens along the (010) and (001) directions, which is less obvious in the slice view. The periods of the underlying correlations along (010) and (001) are about 50 nm. The period along the (011) direction is about 70 nm. The strain gradient along (010) is shown in Fig. 3(c) and

along the (001) direction is shown in Fig. 3(e). The 2D ACF for these two gradients does not show dependence in both directions, as shown in Figs. 3(d) and 3(f). Rather the gradient along (010) shows a 50-nm correlation and the gradient along (001) shows a 65-nm correlation. Note that the spatial resolution of the reconstruction are 18, 22, and 30 nm in X, Y, and Z direction, respectively.

The 2D ACF for Slices 8 and 12 are shown in the Supplemental Material C. The directions and periods of the strain gradients above are compiled together and shown in Table II. The majority of the strain stripes are found along the three {100} directions and always have periods of ∼ 50 nm. We interpret these strain stripes as polar domains or polar nanoregions (PNRs). The idea of PNRs is well-documented in relaxor ferroelectrics, where different models using PNRs have successfully explained the characteristic frequency-dependent properties of the relaxors [44–47]. The definitions of PNRs are diverse for different systems and treated on a case-to-case basis. For example, PNRs are defined in paraelectric $SrTiO_3$ thin films to be the small regions with local polarization which are observed by high angle annular dark field scanning transmission electron microscopy [48]. We propose that PNRs in this work are the small regions with ∼50 nanometers in size and have {100} local polarizations, which is the direction of inner boundaries most often seen in the experiment.

In previous work, BTO samples with tetragonal and cubic global structures were found to have rhombohedral local structures [10–13]. To identify the global and local structures of the commercial BTO samples used in this work, total scattering experiments were done at NSLS II 28-ID-1 beamline. The scattering data from the commercial BTO samples were fitted by four possible BTO crystal structures: cubic (Pm$\bar{3}$m), tetragonal (P4mm), orthorhombic (Amm2), and rhombohedral (R3m). These structural models allow for 5, 14, 20, and 13 structural parameters, respectively. The fittings of the four models in short range, from 0 to 11 Å, are shown in Fig. 4(a). The best fitting results are given by tetragonal P4mm model and orthorhombic Amm2 models, both giving a fit residual error, R_W of 9.7%. The P4mm model is more symmetric than Amm2 model, so the Amm2 model has more degrees of freedom (6 more variables in the fit as compared to tetragonal model). The same error value indicates that additional variables of Amm2 model do not improve the fit quality observably, implying that the tetragonal model with smaller number of parameters is sufficient to explain the data. The other two models give relatively large error, with the cubic Pm$\bar{3}$m $R_W = 14\%$ and rhombohedral $R_W = 16\%$. Small fit discrepancies observed in the r range containing nearest-neighbor correlations including relatively weakly scattering oxygen are prone to termination effects. Achieving more accurate discrimination between the two best
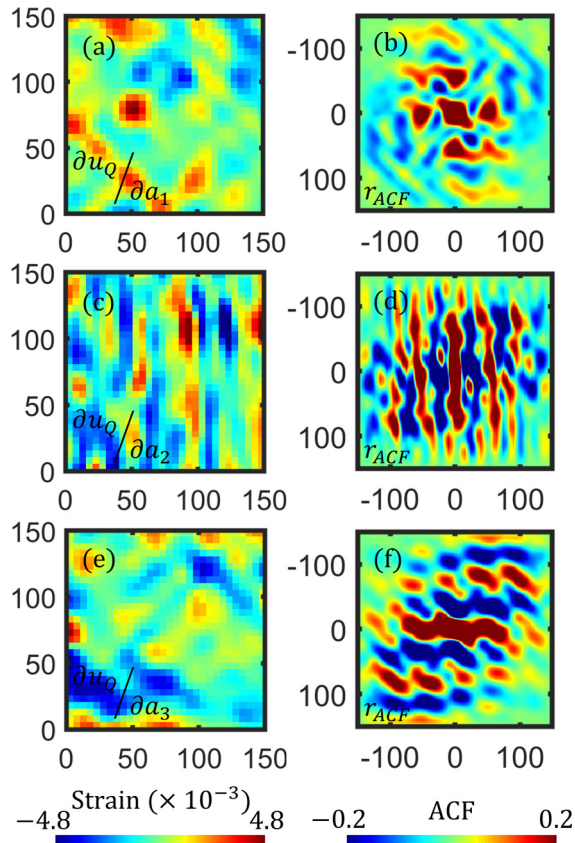

FIG. 3. The 2D ACF is applied to the selected region of the slices shown in Fig. 2. (a), (c), (e) The strain gradients of the selected regions along the (100), (010), and (001) directions, respectively. (b), (d), (f) The 2D ACF of the corresponding gradients. The unit is in nanometer.

TABLE II. The directions and periods of strain stripes shown in Figs. 2, S1, and S2. The Columns represent the periods of the strain stripes, while the rows represent their directions.

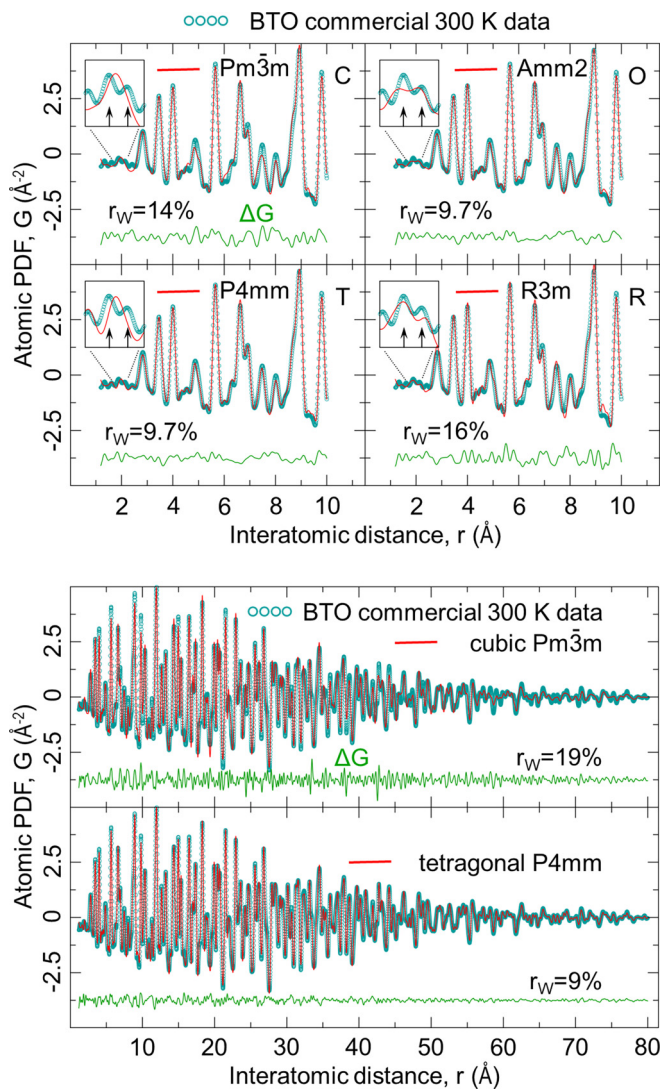|	$\sim$30 nm	$\sim$50 nm	65 $\sim$ 70 nm	90 $\sim$ 120 nm
(100)		$(\frac{\partial u_Q}{\partial a_3})_{a_1 a_3}$		$(\frac{\partial u_Q}{\partial a_1})_{a_1 a_2}$
(010)		$(\frac{\partial u_Q}{\partial a_1})_{a_2 a_3}; (\frac{\partial u_Q}{\partial a_2})_{a_2 a_3}; (\frac{\partial u_Q}{\partial a_2})_{a_1 a_2}$		
(001)		$(\frac{\partial u_Q}{\partial a_1})_{a_2 a_3}; (\frac{\partial u_Q}{\partial a_3})_{a_1 a_3}$	$(\frac{\partial u_Q}{\partial a_3})_{a_2 a_3}$	
(110)				$(\frac{\partial u_Q}{\partial a_3})_{a_1 a_2}$
(101)	$(\frac{\partial u_Q}{\partial a_1})_{a_1 a_3}$			
(10–1)				$(\frac{\partial u_Q}{\partial a_2})_{a_1 a_3}$

FIG. 4. The x-ray PDF of the same powder sample of BTO used throughout this work. The data were collected at NSLS II 28-ID-1 beamline. (a) The short-range fitting of the PDF was done using four crystal structures: cubic (Pm$\bar{3}$m), tetragonal (P4mm), orthorhombic (Amm2) and rhombohedral (R3m). (b) Long-range fitting of the scattering data using two crystal structures: cubic (Pm$\bar{3}$m) and tetragonal (P4mm).

models hence requires utilization of probes with more favorable contrast such as resonant or neutron total scattering. Figure 4(b) shows the fitting of the experimental scattering data to P4mm and Pm$\bar{3}$m model over a longer range, from 0 to 80 Å. The tetragonal P4mm model gives $R_W = 9\%$, while the cubic Pm$\bar{3}$m gives $R_W = 19\%$. Both the short-range and long-range fitting show that the local structure of commercial BTO samples is lower symmetry than cubic.

IV. STRAIN STRIPES NETWORK BEHAVIOR IN BARIUM TITANATE NANOCRYSTALS WHEN CROSSING THE PHASE TRANSITION

To further explore the nature of the strain stripes in Fig. 2, *in situ* BCDI experiments were performed on the selected BTO crystals as a function of temperatures at the ID01 beamline of ESRF.

Two crystals have been studied in detail. The center position of the diffraction peak of the one presented here was found to cross over between the (101) and (110) powder rings. The crystal was measured starting at 100 °C, then the system was heated to 160 °C, after which it was cooled down to 100 °C again so as to cross the cubic-tetragonal phase transition. Figure 5 shows the d spacing vs temperature plot, which was calculated directly from the peak position on the detector (details provided in Supplemental Material D). The d spacing of the diffracted crystal plane was found to decrease a bit during heating from 100 °C to 110 °C. This was followed by a jump in d spacing from 110 °C to 115 °C, which is not well understood. After 120 °C, the d spacing was found to go down approximately linearly until 150 °C, after which the d spacing went up again at a slower rate. We consider the turning point at 150 °C to be a signature of the phase transition temperature, so the negative slope before 150 °C is caused by a decrease of tetragonality, while the positive slope after 150 °C is the thermal expansion of the cubic lattice. When cooling down from 160 °C to 100 °C, the d spacing was seen to reduce approximately linearly with temperature.

Detailed reconstructions were carried out at each temperature following the procedures described above. After reorienting the reconstructed crystal in the calculated crystallographic coordinates, the derivatives of the displacement over the crystallographic axis were taken to get the usual strain tensor components. As before, the three orthogonal
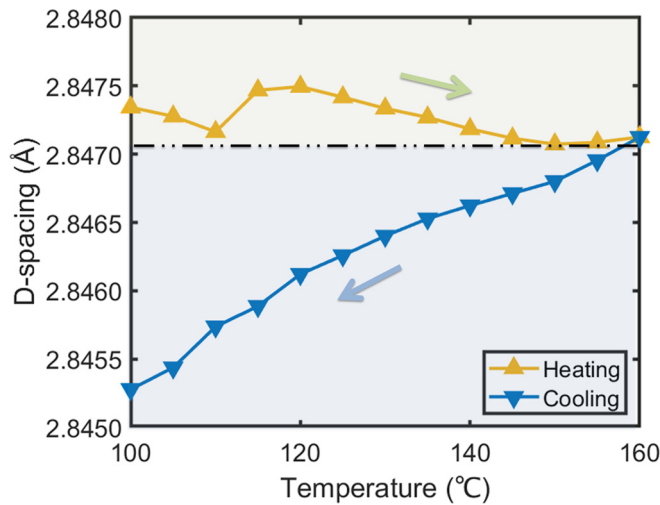
FIG. 5. The d-spacing variations of a BTO crystal during heating and cooling at the ID01 beamline of ESRF.

crystallographic directions are labeled as a_1, a_2, and a_3, being the principal (100), (010), and (001) axes, without knowing which is the c axis.

Figure 6 presents the reconstructed slices (at the same position) showing strain gradients over (010) direction through all the measured temperature points. As can be directly seen, the strain stripes were found to be preserved even as the crystal temperature reached 160 °C. Since the temperature range spanned the phase transition, strain stripes were found to exist inside the crystal no matter whether its phase was tetragonal or cubic. When the crystal was cooled down to 105 °C on the reverse cycle, the strain stripes were still preserved through the phase transition.

Even though the stripes are present at all temperatures their spacing and direction is seen to evolve significantly. To examine the periodicity of the strain stripes qualitatively, the 2D ACFs were evaluated and are shown in Fig. 7 for the strain gradient over (010) direction. In Fig. 7, the period is big and not well defined initially at 100 °C, but gradually becomes clearer upon heating. At 130 °C, the period is well established, with a strong correlation along the diagonal direction, 45° with respect to the (010) and (001) axes. The period is roughly 25 nm. Upon further heating, the period keeps decreasing, coming to roughly 15 nm by 150 °C. Upon further increase of the temperature, the period is constant, but the strong directional correlation along 45° has faded. The crystal gradually forms correlations along both 45° and −45° relative to the (010) axis. Upon cooling down, the correlation along 45° gradually is seen to fade away, while the correlation along −45° became clearer. After cooling to 140 °C, the size of the period has increased to 25 nm and the correlation is strongly distributed along −45°. Further decreasing the temperature, the period increases again in size and becomes less well-defined.

The reconstructed slices containing strain gradients over the (001) direction in Supplemental Material E and their 2D ACF in Supplemental Material F show a similar trend. The 90° switching of the period in both views occurs at roughly the same temperature as the crystal switching from (101) to
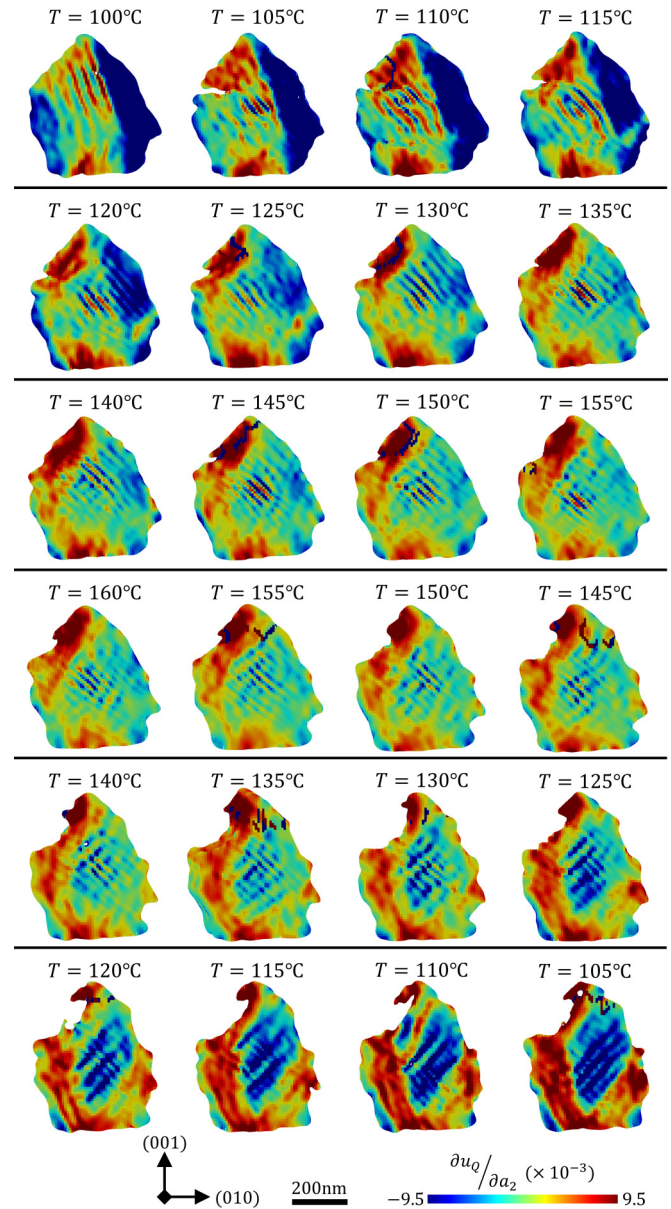

FIG. 6. Central section views of the (100) slices of the strain tensor combinations $^u{}_Q/a_2$ and at every temperature. The crystal went through heating from 100 °C to 160 °C and was then cooled down to 100 °C in 5 °C steps.

(110) powder ring, which corresponds to a 90° switching of the predominant c axis direction in the host crystal lattice. The nice match of the two indicates that the strain stripes are connected to the tetragonal structure. This suggests that the domain walls visualized by the strain stripe could be ferroelectric 90° domain walls. However, ferroelectric domain walls should not exist in a cubic lattice. While the strain stripes are still observable at 160 °C when the crystal has entered cubic phase. If the strain stripes are linked with ferroelectric domain walls, then it supports the idea of a tetragonal local structure in a global cubic crystal phase [19–22]. This question is beyond the scope of this paper and couldn't be answered based on current diffraction data. Future experiments are needed to solve this ambiguity.
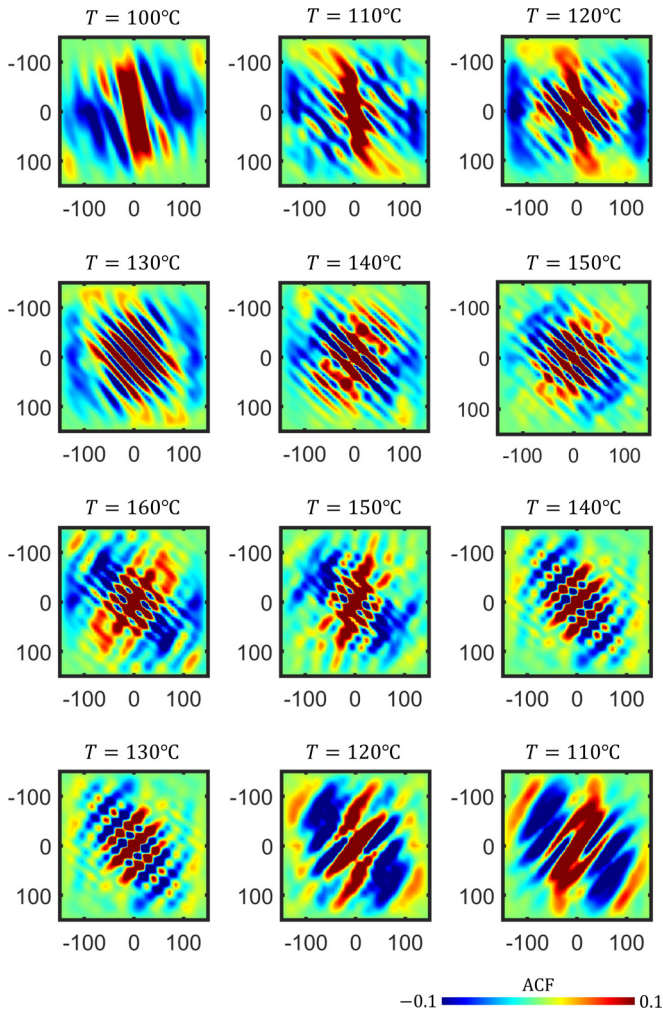
FIG. 7. The 2D ACFs of the strain tensor component $^uQ/_{a_2}$ at every measured temperature.
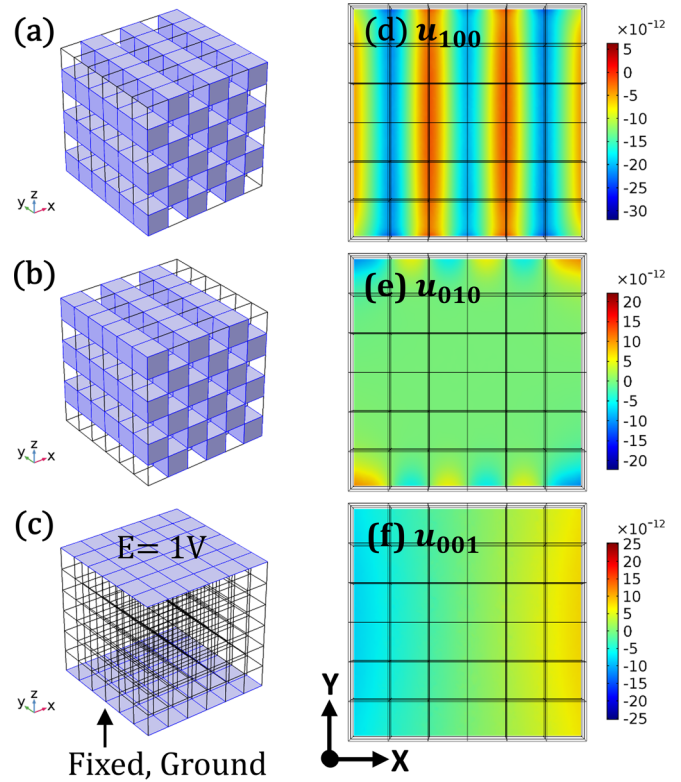

FIG. 8. Results of finite element analysis. (a), (b) The 180° domain definitions. (c) The boundary conditions. (d)–(f) The simulated displacement field in units of meters.

It should be noted that Fourier termination ripples could also result in stripes in the final reconstructed image. These artificial stripes always exist and come from two sources: cropping of the data, which would lead to fringes parallel to the crystal facets; or aliasing of the fast Fourier transform by not having enough zero padding, which gives fringes parallel to the detector edges [49]. To mitigate these possible artifacts, different reconstructions have been performed on the same data with different cropping and zero padding. Cropping led to a small subtle variation of stripes in the final images, far too small to explain the data. Reconstruction of the same data with different zero padding showed negligible differences. Therefore, we conclude the stripe images in this work are physically real and not coming from data cropping or aliasing.

V. FINITE ELEMENT ANALYSIS SIMULATION

The finite element analysis (FEA) method was used to simulate the strain stripes observed in the 300 nm BTO nanocrystals to understand their origin. FEA is a numerical method to solve general physical and engineering problems defined by coupled differential equations in 3D space. This involves subdividing the entity into small units and solving the

partial differential equations of the mechanical deformation of these smaller units under defined external conditions and boundary conditions. In our simulation using the COMSOL package, different geometries, domain combinations, and configurations were built and solved by FEA to generate and visualize the strain pattern. The goal was to compare the simulated strain patterns with the experimental results in order to verify which model works in an attempt to understand the origin of the observed strains. Several different domain models were tried; only the one closest to the experimental result is presented here, with some other examples presented in the Supplemental Material.

180° domains are widely found in tetragonal BTO crystals. The only structure difference between the two adjacent domains is that the Ti^{4+} displacement directions are opposite, and so are the polarizations. In this work, different piezoelectric coefficients were used to define primary blocks representing different polarizations. The details are shown in Supplemental Material H.

The 180° domain definitions are shown in Figs. 8(a) and 8(b), while the boundary conditions are shown in Fig. 8(c). The simulations were then performed, and the simulated displacements were calculated. Figures 8(d) to 8(f) shows three orthogonal displacement field in one XY slice. The displacement field in u_{100}, accumulated along the vertical direction has stipes of magnitude 10^{-12} m, which are not seen in other two displacement fields.
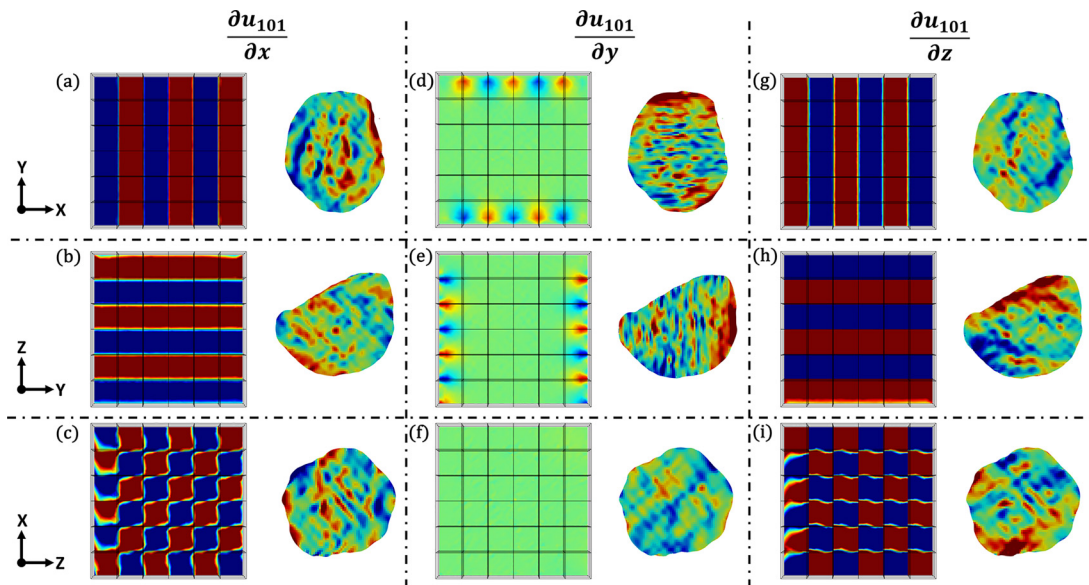
FIG. 9. The simulated strain field are compared with experimental images. In (a)–(i), the left cubes show the simulated strain distribution, while the right crystal slices show the reconstructed strain.

The relevant combination of the strain tensors given in Eqs. (2)–(4) were added together to simulate the accessible BCDI strain fields. Figure 9 shows a side-by-side view of the simulated results and the crystal in Fig. 1. Of all the nine views to show the simulated strain distributions, two views show vertical strain stripes, and another two views show horizontal strain stripes. There are another two views showing strain stripes along the diagonal, 45° inclined to the X and Z direction. The remaining three views have weak strain distributions. A convergence study was also performed to confirm the appropriate precision of the meshing grids, which is presented in the Supplemental Material G.

Other domain models were also simulated and tested, some of which are listed in Supplemental Material I. The best fitting 180° domain wall model, shown in Figs. 8 and 9, has horizontal, vertical, and diagonal strain stripe distributions, all of which are seen in the strain images of the crystal studied in Fig. 2. It should be noted that even the best fitting model only partially matches the experimental results. Most views have their horizontal, vertical, and diagonal strain stripe directions matched, but others do not.

VI. CONCLUSION

In this work, a 3D network of strain stripes with $30 \sim 50$ nm spacing has been revealed inside BTO nanocrystals by BCDI. As far as we know, these have not been reported before and may be unique to nanometer-sized materials. Since relatively few experimental techniques have the sensitivity and resolution in 3D to identify these features, which are attributed to ferroelectric domains, they may be a general property of crystalline BTO. The crystal facets were used to establish the crystallographic axis directions. The strain components were then calculated along those directions. For the crystal measured at APS 34-ID-C at room temperature, the directions of the strain stripes were mostly along {100} or {110}. The

2D ACF was evaluated in selected regions to quantitatively measure the stripe periods, which ranged from 30 to 50 nm.

An annealing BCDI experiment was then performed at ESRF ID01, where a different crystal was heated up to the cubic phase and cooled down to the tetragonal phase again. During the process, the diffraction pattern was found to move from the (101) powder ring to the (110) powder ring, indicating a reorientation of the c axis after crossing the phase transition. The slice views through the BCDI reconstructions show that the strain stripes inside the crystal also change their direction through the heating and cooling. This match of c axis reorientation and strain stripe direction switching suggests that the strain stripes come from the ferroelectric domain walls. However, there was some residue of the stripe pattern with a different spacing and orientation in the cubic phase as well.

To understand the ferroelectric strain stripes, different models have been built to simulate them. While both 90° and 180° domains configurations give stripes due to strain, the 180° domains model seems to work better. It has six views out of nine views showing {001} or {110} directional stripes. Our discovery of strain stripes in nanocrystalline BTO may have significant implications for the understanding of relaxor ferroelectric materials, which are predicted to contain nano polar regions.

[1] V. Garcia, S. Fusil, K. Bouzehouane, S. Enouz-Vedrenne, N. D. Mathur, A. Barthélémy, and M. Bibes, Giant tunnel electroresistance for non-destructive readout of ferroelectric states, Nature (London) **460**, 81 (2009).

[2] K. H. Noh, B. Yang, S. W. Lee, S. S. Lee, H. B. Kang, and Y. J. Park, Issues and reliability of high-density FeRAMs, Jpn. J. Appl. Phys. **42**, 2096 (2003).

[3] A. von Hippel, Ferroelectricity, domain structure, and phase transitions of barium titanate, Rev. Mod. Phys. **22**, 221 (1950).

[4] F. Jona and G. Shirane, *Ferroelectric Crystals* (Pergamon Press, London, 1962).

[5] Q. Zhang, T. Cagin, and W. A. Goddard, The ferroelectric and cubic phases in $BaTiO_3$ ferroelectrics are also antiferroelectric, Proc. Natl Acad. Sci. **103**, 14695 (2006).

[6] B. D. Stojanovic, C. Jovalekic, V. Vukotic, A. Z. Simoes, and J. A. Varela, Ferroelectric properties of mechanically synthesized nanosized barium titanate, Ferroelectrics **319**, 65 (2005).

[7] W. David Kingery, H. K. Bowen, and D. R. Uhlmann, *Introduction to Ceramics* (Wiley, New York, 1976).

[8] R. E. Cohen, Origin of ferroelectricity in perovskite oxides, Nature (London) **358**, 136 (1992).

[9] G. Catalan, A. Lubk, A. H. G. Vlooswijk, E. Snoeck, C. Megan, A. Janssens, G. Rispens, G. Rijnders, D. H. A. Blank, and B. Noheda, Ferroelectric rotation of polarization in ferroelectric thin film, Nat. Mater. **10**, 963 (2011).

[10] G. Catalan, J. Seidel, R. Ramesh, and J. F. Scott, Domain wall nanoelectronics, Rev. Mod. Phys. **84**, 119 (2012).

[11] J. Diao, X. Shi, T. A. Assefa, L. Wu, A. F. Suzana, D. S. Nunes, D. Batey, S. Cipiccia, C. Rau, R. J. Harder, W. Cha, and I. K. Robinson, Evolution of ferroelastic domain walls during phase transitions in barium titanate nanoparticles, Phys. Rev. Mater. **4**, 106001 (2020).

[12] T. Hoshina, H. Kakemoto, T. Tsurumi, S. Wada, and M. Yashima, Size and temperature induced phase transition behaviors of barium titanate nanoparticles, J. Appl. Phys. **99**, 054311 (2006).

[13] W. Y. Shih, W. H. Shih, and I. A. Aksay, Size dependence of the ferroelectric transition of small BaTiO3 particles: Effect of depolarization, Phys. Rev. B **50**, 15575 (1994).

[14] W. R. Buessem, L. E. Cross, and A. K. Goswami, Effect of two-dimensional pressure on the permittivity of fine- and coarse-grained barium titanate, J. Am. Ceram. Soc. **49**, 36 (1966).

[15] G. Arlt, D. Hennings, and G. De With, Dielectric properties of fine-grained barium titanate ceramics, J. Appl. Phys. **58**, 1619 (1985).

[16] S. Wada, H. Yasuno, T. Hoshina, S. M. Nam, H. Kakemoto, and T. Tsurumi, Preparation of nm-sized barium titanate fine particles and their powder dielectric properties, Jpn. J. Appl. Phys. **42**, 6188 (2003).

[17] T. Hoshina, S. Wada, Y. Kuroiwa, and T. Tsurumi, Composite structure and size effect of barium titanate nanoparticles, Appl. Phys. Lett. **93**, 2006 (2008).

[18] T. Hoshina, Size effect of barium titanate: Fine particles and ceramics, J. Ceram. Soc. Jpn. **121**, 156 (2013).

[19] D. A. Keen and A. L. Goodwin, The crystallography of correlated disorder, Nature (London) **521**, 303 (2015).

[20] G. H. Kwei, S. J. L. Bilinge, S. -W. Cheong, and J. G. Saxton, Pair-distribution functions of ferroelectric perovskites: Direct observation of structural ground states, Ferroelectrics **164**, 57 (1995).

[21] M. S. Senn, D. A. Keen, T. C. A. Lucas, J. A. Hriljac, and A. L. Goodwin, Emergence of long-range order in $BaTiO_3$ from local symmetry-breaking distortions, Phys. Rev. Lett. **116**, 207602 (2016).

[22] J. R. Neilson and T. M. McQueen, Representational analysis of extended disorder in atomistic ensembles derived from total scattering data, J. Appl. Crystallogr. **48**, 1560 (2015).

[23] I. Robinson and R. Harder, Coherent x-ray diffraction imaging of strain at the nanoscale, Nat. Mater. **8**, 291 (2009).

[24] F. Hofmann, E. Tarleton, R. J. Harder, N. W. Phillips, P. W. Ma, J. N. Clark, I. K. Robinson, B. Abbey, W. Liu, and C. E. Beck, 3D lattice distortions and defect structures in ion-implanted nano-crystals, Sci. Rep. **7**, 45993 (2017).

[25] G. Xiong, O. Moutanabir, M. Reiche, R. Harder, and I. Robinson, Coherent x-ray diffraction imaging and characterization of strain in silicon-on-insulator nanostructures, Adv. Mater. **26**, 7747 (2014).

[26] J. N. Clark, J. Ihli, A. S. Shpyrko, Y.-Y. Kim, A. N. Kulak, J. M. Campbell, G. Nisbet, F. C. Meldrum, and I. Robinson, Three-dimensional imaging of dislocation propagation during crystal growth and dissolution, Nat. Mater. **14**, 780 (2015).

[27] A. Ulvestad, A. Singer, J. N. Clark, H. M. Cho, J. W. Kim, R. Harder, J. Maser, Y. S. Meng, and O. G. Shpyrko, Topological defect dynamics in operando battery nanoparticles, Science **348**, 1344 (2015).

[28] https://www.scbt.com/p/barium-titanate-iv-nanopowder-200-nm-particle-size-12047-27-7.

[29] J. Miao, D. Sayre, and H. N. Chapman, Phase retrieval from the magnitude of the Fourier transforms of nonperiodic objects, J. Opt. Soc. Am. A **15**, 1662 (1998).

[30] J. Miao, P. Charalambous, J. Kirz, and D. Sayre, Extending the methodology of x-ray crystallography to allow imaging of micrometer-sized non-crystalline specimens, Nature (London) **400**, 342 (1992).

[31] J. R. Fienup, Phase retrieval algorithms: A comparison, Appl. Opt. **21**, 2758 (1982).

[32] J. P. Abrahams and A. G. W. Leslie, Methods used in the structure determination of bovine mitochondrial F1 ATPase, Acta Crystallogr. D **52**, 30 (1996).

[33] D. R. Luke, Relaxed averaged alternating reflections for diffraction imaging, Inverse Prob. **21**, 37 (2005).

[34] H. H. Bauschke, P. L. Combettes, and D. R. Luke, Phase retrieval, error reduction algorithm, and Fienup variants: A view from convex optimization, J. Opt. Soc. Am. A **19**, 1334 (2002).

[35] H. H. Bauschke, P. L. Combettes, and D. R. Luke, Hybrid projection-reflection method for phase retrieval, J. Opt. Soc. Am. A **20**, 1025 (2003).

[36] See Supplemental Material at http://link.aps.org/supplemental/10.1103/PhysRevMaterials.8.016002 for the introduction of shrink-wrap, which is a support updating method; So is the guided algorithm technique, which is widely used in this work. It also contain Refs. [37–39].

[37] S. Marchesini, A unified evaluation of iterative projection algorithms for phase retrieval, Rev. Sci. Instrum. **78**, 011301 (2007).

[38] L. Li, Y. Xie, E. Maxey, and R. Harder, Methods for operando coherent x-ray diffraction of battery materials at the Advanced Photon Source, J. Synchrotron Radiat. **26**, 220 (2019).

[39] M. B. Smith, K. Page, T. Siegrist, P. L. Redmond, E. C. Walter, R. Seshadri, L. E. Brus, and M. L. Steigerwald, Crystal structure and the paraelectric-to-ferroelectric phase transition of nanoscale BaTiO$_3$, J. Am. Chem. Soc. **130**, 6955 (2008).

[40] H. P. Bonzel and K. Duckers, *Relationship Between Anisotropy of Specific Surface Free Energy and Surface Reconstruction* (Springer-Verlag, Berlin, 1988).

[41] J. Ahrens, B. Geveci, and C. Law, *ParaView: An End-User Tool for Large Data Visualization, Visualization Handbook* (Elsevier, Amsterdam, 2005).

[42] F. Hoffman, B. Abbey, W. Liu, R. Xu, B. F. Usher, E. Balaur, and Y. Liu, X-Ray micro-beam characterization of lattice rotations and distortions due to an individual dislocation, Nat. Commun. **4**, 2774 (2013).

[43] J. D. Hamilton, *Time Series Analysis* (Princeton University Press, Princeton, NJ, 1994).

[44] G. E. P. Box, G. N. Jenkins, G. C. Reinsel, and M. G. Ljung, *Time Series Analysis: Forecasting and Control*, 5th ed. (Wiley, Hoboken, NJ, 2016).

[45] M. Eremenko, V. Krayzman, A. Bosak, H. Y. Playford, K. W. Chapman, J. C. Woicik, B. Ravel, and I. Levin, Local atomic order and hierarchical polar nanoregions in a classical relaxor ferroelectric, Nat. Commun. **10**, 2728 (2019).

[46] D. Fu, H. Taniguchi, M. Itoh, S. Koshihara, N. Yamamoto, and S. Mori, Relaxor Pb(Mg$_{1/3}$Nb$_{2/3}$)O$_3$: A ferroelectric with multiple inhomogeneities, Phys. Rev. Lett. **103**, 207601 (2009).

[47] F. Li, S. Zhang, T. Yang, Z. Xu, N. Zhang, G. Liu, J. Wang, J. Wang, Z. Cheng, Z. Ye, J. Luo, T. R. Shrout, and L. Q. Chen, The origin of ultrahigh piezoelectricity in relaxor-ferroelectric solid solution crystals, Nat. Commun. **7**, 13807 (2016).

[48] D. Lee, H. Lu, Y. Gu, S. Y. Choi, S. D. Li, S. Ryu, T. R. Paudel, K. Song, E. Mikheev, S. Lee, S. Stemmer, D. A. Tenne, S. H. Oh, E. Y. Tsymbal, X. Wu, L. Q. Chen, A. Gruverman, and C. B. Eom, Emergence of room-temperature ferroelectricity at reduced dimensions, Science **349**, 1314 (2015).

[49] Y. Gao, X. Huang, H. Yan, and G. J. Williams, Bragg coherent diffraction imaging by simultaneous reconstruction of multiple diffraction peaks, Phys. Rev. B **103**, 014102 (2021).

[50] https://data.esrf.fr/doi/10.15151/ESRF-ES-407021311.